Impact of Mn-substitution on structural, optical, and magnetic properties evolution of sodium–cobalt ferrite for opto-magnetic applications

Amany M. ElNahrawy[1] · A. M. Mansour[1] · Hoda A. ElAttar[2] · Elham M. M. Sakr[2] · Aisha A. Soliman[2] · Ali B. Abou Hammad[1]

Abstract

Mixed-metal oxide spinel ferrite nanoparticles of composition $Na_{0.5}Mn_xCo_{(0.5-x)}Fe_2O_4$ (where $x = 0.0$, 0.1, 0.3, and 0.5) were synthesized successfully through a well-known citrate sol–gel autocombustion method. X-ray diffraction approach, transmission electron microscope, scanning electron microscope, and spectroscopic Fourier transform infrared were used to investigate the microstructure and the formation of the composites. Diffuse reflectance was employed to investigate the optical properties and estimating of optical band gap type and value. The magnetic analysis was made by employing a vibrating sample magnetometer. It was found that the average crystallite size increases with the increase of manganese (Mn) content. The formation of the spinel structure of Mn-doped Na-CFO was confirmed by FTIR spectra. The direct optical band gap was observed through the Kubelka–Munk function calculation of diffusely reflected light. The saturation magnetization decreases with the addition of Mn cations.

1 Introduction

In the past few years, significant efforts were made to establish magnetic nanoparticles (MNPs), understand their behavior, and enhance their validity in several applications [1]. Accurate monitoring of MNPs' preparation conditions and surface properties is essential because it regulates their physicochemical characteristics, their stability, and their functionality [2]. A further important parameter is a possibility to adapt their surface composition to enable their features to be produced according to the desired request. This class of nanomaterials has fostered innovation in a multitude of study fields, particularly in the fields of environmental management, biomedicine, magnetic cooling, catalysis, and microwave devices [3–7]. Mixed-metal oxide spinel-type systems are highly flexible,which can be used as catalysts for a multitude of reactions. They are now being explored for redox reactions containing biomass-derived base parts directed at producing either chemicals or fuel products due to their various chemical--physical characteristics [8]. Because of their notable magnetic, electrical, and optical characteristics, spinel ferrite nanoparticles (MFe_2O_4, where M(II), a d-block transition metal) are promising components for the growth of new techniques [2]. Among the various spinel-type ferrite structures, exceptional attention is given to nanostructured $MnFe_2O_4$ and $CoFe_2O_4$ as another choice to magnetite (Fe_3O_4) owing to its high chemical oxidation resistance and essential magnetic features [9]. $MnFe_2O_4$ became extremely important for biotechnology requests due to its improved magnetization of distortion related to other nano-ferrites [10]. Additionally, because of its elevated resistance to magnetization change and anisotropy of its magnetocrystalline, $CoFe_2O_4$ is one of the favored substrates for high-density data storage and stress detecting purposes [11].

However, the configuration of Co(II)- and Mn(II)-based ferrite superparamagnetic nanoparticles, having structural, magnetic, and electrical features customized for each particular application, remains demanding for researchers. Several types of research were focused on nano-ferrite's rational design with controllable, predictable, and

✉ A. M. Mansour
amamansour@gmail.com

1   Solid State Physics Department, Physics Research Division, National Research Centre, 33 El Bohouth St., Dokki, Giza 12622, Egypt

2   Department of Solid State Physics, Faculty of Women for Arts, Science and Education, Ain Shams University, Cairo, Egypt

reproducible properties, particularly for manufacturing [12]. Regular investigations were reported on the effect of size, shape, surface functionality, and interparticle interactions on the magnetic characteristics of these spinel ferrite nanoparticles. A statistical factor modeling method has been created to mathematically align the size of $CoFe_2O_4$ with the microemulsion experimental conditions [13]. By varying the reaction settings, or by seed growth during the thermal decomposition process, a tunable size of 3–20 nm of $MnFe_2O_4$ and $CoFe_2O_4$ was prepared [14]. Currently, $Co_xMn_{1-x}Fe_2O_4$ ($x = 0–1$) nano-ferrites have appeared as a potential approach to enhance their performance. In addition, for the preparation of other mixed spinel systems, including $Zn_xMn_{1-x}Fe_2O_4$, $Zn_xFe_{1-x}Fe_2O_4$ [15], and $Ni_{1-x}Zn_xFe_2O_4$ [16], the ability of such strategy to enhance the structure, surface, and magnetic appearances was outlined.

Different preparation ways of mixed ferrites have been noted, like thermal decomposition, chemical auto combustion, polyol method, hydrothermal, solid-state reactions, seed growth method, precursor technique, and citrate-sol–gel autocombustion [8]. The sol−gel autocombustion procedure is based on the hydroxylation and condensation of a liquid precursor to produce a sol of nanosized units [17, 18]. Sol condensation mechanisms give a network of metal oxide gel [19]. By drying and calcination of the produced gel, the crystalline form is acquired. Through the controlling of the hydroxylation and condensation factors, the desired features and composition of the gel can be readily attained [20]. In particular, the pH, heat, used salt nature, concentration, and the used solvent are the main factors that impact the synthesis process [17, 21].

Spinel ferrites having dielectric, electrical, and magnetic characteristics are extremely sensitive to the manufacturing process and its conditions, including composition and impurity ratio of used chemicals and heat treatment. Transition and diamagnetic metal ion substitution in spinel ferrites are a popular and effective strategy for enhancing magnetization ability and effecting permittivity and permeability by frequencies [22]. In this work, $Na_{0.5}Mn_xCo_{(0.5-x)}Fe_2O_4$ (where $x = 0.0, 0.1, 0.3,$ and 0.5) nanoparticle synthesis through the sol–gel autocombustion method methodology was reported. The concern here is to study the structural, optical, and magnetic properties that are given and discussed to perfectly understand the behavior of these $Na_{0.5}Mn_xCo_{(0.5-x)}Fe_2O_4$ magnetic particles for opto-magnetic applications. The microstructure and composition analysis were investigated by XRD spectroscopy, transmission electron microscopy (TEM), scanning electron microscopy (SEM), and Fourier transform infrared spectroscopy (FTIR). The optical band

gap and its type were investigated by the reflectance spectroscopy method. The magnetic properties were analyzed by the vibrating sample magnetometer (VSM).

2 Experimental work

2.1 Materials used and preparation steps

A series of Mn-doped Na–cobalt ferrite nanomagnetic particles having the formula $Mn_xNa_{0.5}Co_{(0.5-x)}Fe_2O_4$ (where $x = 0.0, 0.1, 0.3, 0.5$) were synthesized by a citrate sol–gel autocombustion method at room temperature. Magnetic nanoparticles were synthesized by taking manganese(II) acetate tetrahydrate ($C_4H_6MnO_4 \cdot 4H_2O$), sodium nitrate ($NaNO_3$), cobalt nitrate ($Co(NO_3)_2 \cdot 6H_2O$), and iron nitrate ($Fe(NO_3)_3 \cdot 9H_2O$) as precursors and citric acid as a fuel. In the case of substitution, the nitrate of the substituted element was taken. First stoichiometry amounts metal nitrates (as 0.1:0.5:0.4:2, 0.3:0.5:0.2:2, and 0.5:0.5:0.0:2) were dissolved in distilled water separately and citric acid was dissolved in a separate beaker. Finally, the three solutions are mixed under vigorous magnetic stirring and the final solution was simultaneously heated at 100 °C under vigorous magnetic stirring. Because of heating, water evaporates and viscous liquid forms which automatically combusts to give brownish-black fluffy powder. This powder was ground and calcined at 800 °C for 3 h in the open air to obtain a dense nano-powder of pure and Mn-doped Na-CFO.

2.2 Characterization techniques

The structural investigation of the prepared $Na_{0.5}Mn_xCo_{(0.5-x)}Fe_2O_4$ (where $x = 0.0, 0.1, 0.3,$ and 0.5) mixed-metal spinel ferrite nanoparticles was carried out by X-ray Bruker-D8 advance diffractometer (XRD) using monochromatized CuKα radiation of wavelength (λ) = 1.54056 Å operated at 40 kV and 40 mA. The surface morphology and structural shape of prepared mixed-metal spinel ferrite were performed by employing both the scanning electron microscope (JEM-1230) and transmission electron microscope (JEOL, JEM-2100). Fourier transform infrared (FTIR) spectra of the prepared samples were recorded with an FTIR spectrometer (Nicolet Impact-400 FTIR spectrophotometer) in the range of 200–4000 cm^{-1}. Optical diffusion was carried out by a (Jasco-V-570) spectrophotometer (Jasco; USA), in the wavelength range of 0.2–2.0 μm. Room-temperature magnetic hysteresis loops were measured by vibrating sample magnetometer (VSM Model: Lakeshore 7410).
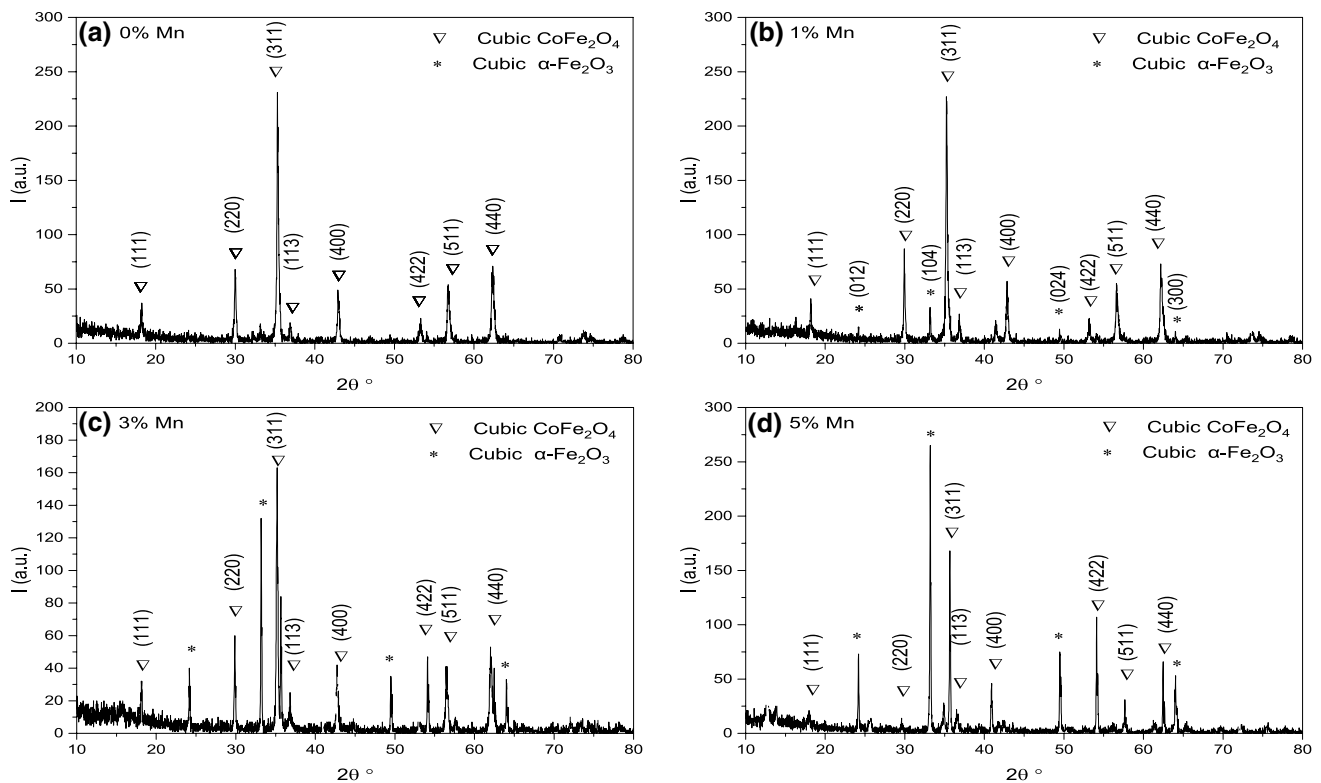
**Fig. 1** The XRD patterns for $Mn_xNa_{0.5}Co_{(0.5-x)}Fe_2O_4$ with **a** $x = 0.0$, **b** $x = 0.1$, **c** $x = 0.3$ and **d** $x = 0.5$, calcined at 800 °C

3 Results and discussion

3.1 X-ray diffraction (XRD) analysis

Figure 1 shows the XRD patterns of $Na_{0.5}Co_{0.5}Fe_2O_4$ (Na-CFO) and $Mn_xNa_{0.5}Co_{(0.5-x)}Fe_2O_4$ (where $x = 0.1$, 0.3, and 0.5) nanostructure samples prepared using effective sol–gel autocombustion process. The resulted XRD patterns confirmed the presence of the spinel CFO phase and revealed its crystallinity for all studied samples. For all samples, Fig. 1a–d shows the XRD results, where the peaks at positions 18.24°, 30.03°, 35.29°, 36.98°, 43.01°, 53.36°, 56.75°, and 62.43°refer to the planes (111), (220), (311), (113), (400), (422), (511), and (440), respectively. These results indicate the formation of a single-phase spinel cubic structure of Na-CFO with space group Fd3m (in accordance with JCPDS, Card no. 22-1086) of the cubic $CoFe_2O_4$. For the Co-doped samples, i.e. 0.1%, 0.3%, and 0.5% as shown in Fig. 1b–d, respectively, there is a trace of secondary phase which was located at positions 24.18, 33.17, 49.45, and 64.04corresponding to the planes (012), (104), (024), and (300) of hematite (α-Fe_2O_3), (in accordance with JCPDS, Card no. 03-0800). This secondary phase of α-Fe_2O_3 has a body-centered cubic (BCC) structure and therefore is not easily softened into the ferrite phase of face-centered cubic (FCC) structure; so the traces

of this corresponding secondary phase can easily be identified in X-ray diffraction patterns [23]. The appearance of the second phase may be attributed to the transformation of Mn^{2+} at A-sites to Mn^{3+} at B-sites and vice versa for Fe^{3+} at B-sites to Fe^{2+} at A-sites [24]. The formation of hematite with increasing Mn content can be attributed to the decomposition of $MnFe_2O_4$ to αFe_2O_3 and Mn_2O_3 according to the following equation:

$$2MnFe_2O_4 + O \rightarrow Mn_2O_3 + 2\alpha Fe_2O_3$$
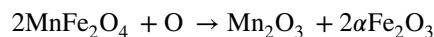
This decomposition occurs under the effect of oxygen environment during the heat treatment process, where the environmental oxygen plays a fatal role in the oxidation state of Mn and Fe which leads to the decomposition of $MnFe_2O_4$ [25]. It has been reported that these secondary phases are absent in as-prepared and sintered samples of above 1000 °C [26]. The average crystallite size of the prepared samples (D) was calculated for the most intense peaks of each sample by Sherrer's formula. The estimated crystallite size was found to be about 26, 23, 35, and 40 nm for (Na-CFO), ($Mn_{0.1}Na_{0.5}Co_{0.4}Fe_2O_4$), ($Mn_{0.3}Na_{0.5}Co_{0.2}Fe_2O_4$), and ($Mn_{0.5}Na_{0.5}Fe_2O_4$), respectively. There is a small shift in the position of the peak (311) to a lower 2θ value for ($Mn_{0.1}Na_{0.5}Co_{0.4}Fe_2O_4$) and ($Mn_{0.3}Na_{0.5}Co_{0.2}Fe_2O_4$),

indicating the increase in the lattice parameter due to the difference in ionic radii of Mn^{2+} (0.8 Å) and Co^{2+} (0.745 A°) according to Vegard's law [27]. Also, there is a relative decrease in the intensity of all the peaks of the cubic spinel structure for all the samples, corresponding to the incorporation of Mn^{2+} ions in pure (Na-CFO) network. This is maybe imputed to the decrease of the total molecular weight of the prepared nanomagnetic samples by the introduction of the lighter Mn^{2+} ions than Co^{2+} ions in (Na-CFO) nanostructure. However, as the Mn^{2+} ions content increase to the maximum value ($x = 0.5$) in which all the Co^{2+} ions are substituted by Mn^{2+} ions, the peak (311) is shifted to a higher value indicating an obvious decrease in the lattice parameter. This is can be explained by the action of secondary phase segregation on the grain boundary which is considered one of the microstrain sources in the lattice [28]. Noticeably, there is an increase in the intensity of the peaks of the secondary phase referring to the high crystallinity

and enhancement of hematite structure. We can also notice that at the beginning of doping our host system with Mn^{2+} ions ($x = 0.1$), the crystallite size decreases and by an excess amount of Mn^{2+} ions ($x = 0.3$ and 0.5), the crystallite size begins to increase sharply, due to the incorporation of the larger Mn^{2+} ions in the lattice will produce a microstrain which will decrease the crystallite size [29]. But, increasing the Mn^{2+} ion content is accompanied by the formation of the second phase, which decreases the lattice strain and hence the crystallite size begins to increase. The estimated values of average crystallite sizes (D in nm), lattice parameters (a in Å), and strain are tabulated in Table 1.

3.2 TEM images

Figure 2 shows the TEM images of the prepared $Mn_xNa_{0.5}Co_{(0.5-x)}Fe_2O_4$ (where x = 0.1 and 0.3) nanoparticles calcined at 800 °C, which indicate the common

Table 1 The values of crystallite size (D) and lattice parameter (a) with the substitution of Mn^{2+} ions into Na-CFO

Sample	Crystallite size (D) (nm)	d-spacing (Å)	Exp. Lattice parameter (Å)	Theo. lattice parameter (Å)	Molecular weight (a.m.u)	X-ray density g/cm³	Specific surface area (m²/g)	Strain (ε)
$Na_{0.5}Co_{0.5}Fe_2O_4$	26.3	2.5424	8.4422	8.4220	216.649	4.800	47.529	0.275
$Mn_{0.1}Na_{0.5}Co_{0.4}Fe_2O_4$	23	2.546	8.4435	8.4332	216.250	4.772	54.667	0.330
$Mn_{0.3}Na_{0.5}Co_{0.2}Fe_2O_4$	35.3	2.5505	8.4589	8.4487	215.451	4.729	35.942	0.221
$Mn_{0.5}Na_{0.5}Fe_2O_4$	39.6	2.5170	8.3479	8.3378	214.652	4.902	30.909	0.272

Fig. 2 TEM images of **a**, **b** $Mn_{0.1}Na_{0.5}Co_{0.4}Fe_2O_4$ at two magnifications powers and **c** $Mn_{0.3}Na_{0.5}Co_{0.2}Fe_2O_4$ nanoparticles, calcined at 800 °C for 3 h
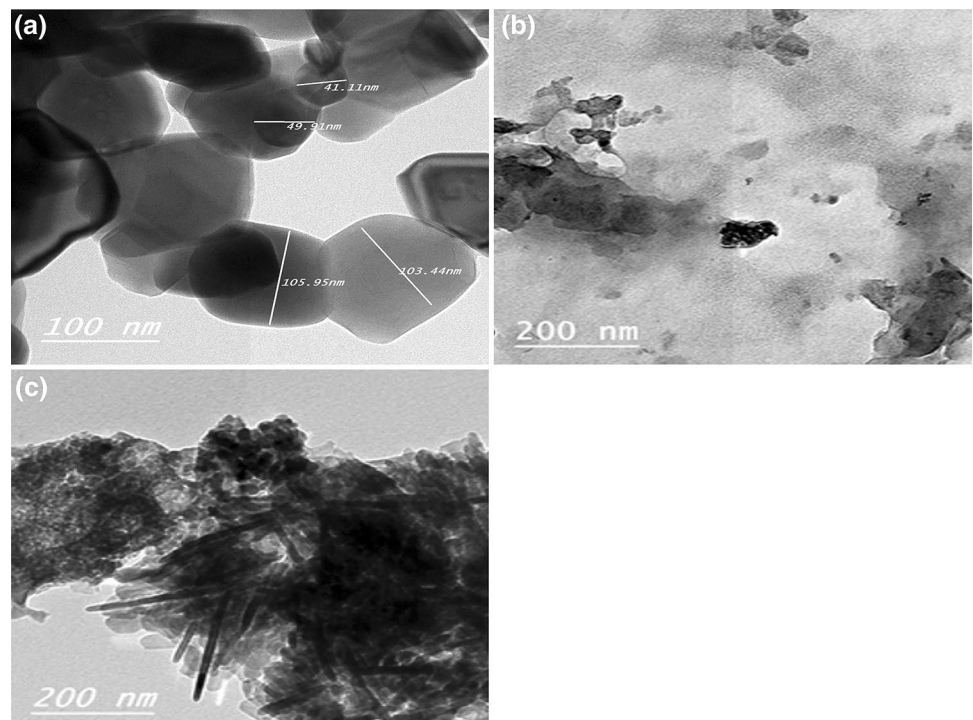
nano-scale nature of the prepared magnetic matrix. Figure 2a, b reveals a homogeneous distribution of nano-cubic and nano-spheres with almost an average particle size of 20 nm up to 40 nm. Particle growth enhancement by increasing Mn content has been observed as shown in Fig. 2c. The nano-spheres were found to have approximate sizes of 25 nm as indicated in its particle size distribution histogram. Also, a nano-rods with a diameter of about 11 nm. The high agglomeration observed in these TEM images is mainly due to their magnetic nature. These results are in good agreement with the XRD measurements.
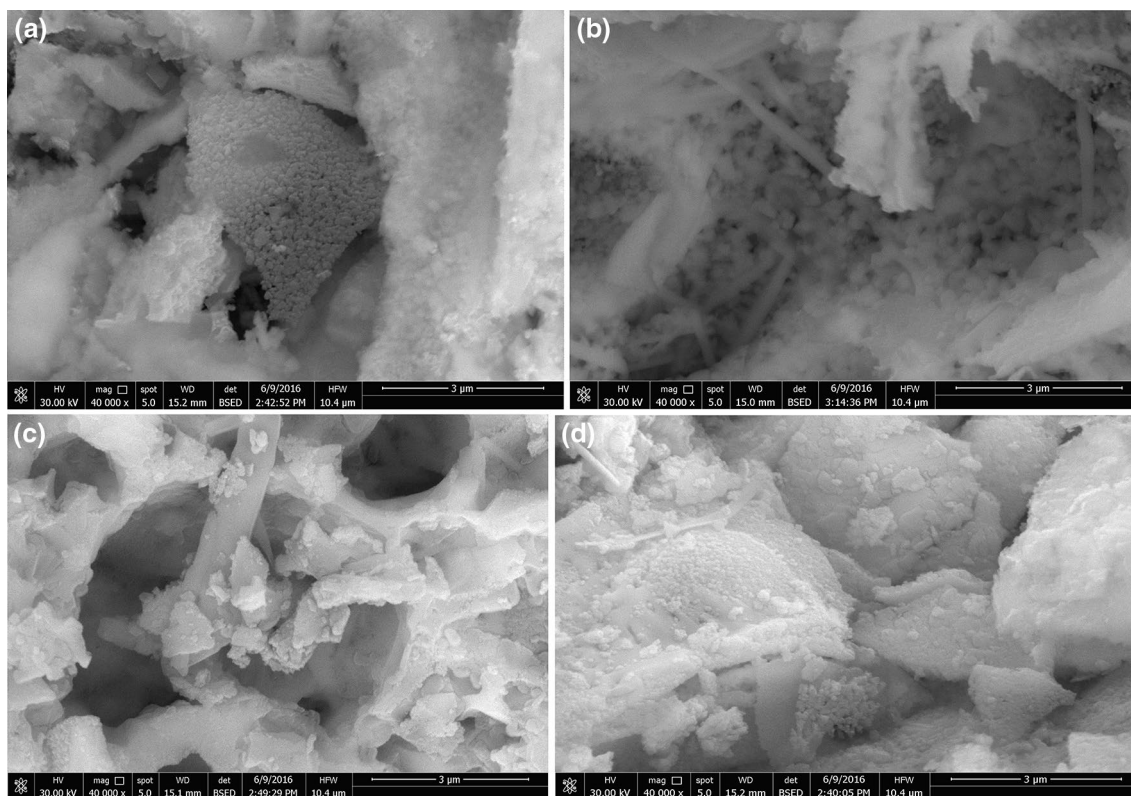
3.3 SEM images

The surface morphology of the samples $Mn_xNa_{0.5}Co_{(0.5-x)}Fe_2O_4$ (where $x=0.1$, 0.3, and 0.5), calcined at (800 °C) for 3 h as shown in Fig. 3, has been studied by the use of high-resolution scanning electron microscopy (SEM). Figure 3 shows the SEM images of the Mn/Na$_{0.5}$Co$_{0.5}$Fe$_2$O$_4$ samples, which exhibits a spongy and high homogeneous surface. By increasing the Mn content as shown in Fig. 3b, d, the SEM images exhibit a smoothed surface formed from some nano-rods and nano-spheres with a higher degree of porosity, and the particle nanosizes are nearly less than 60 nm. The presence of the holes and

nano-porous features in the Mn–Na-CFO surface could be ascribed to the successful formation during the calcination process at 800 °C. The SEM values of nanoparticle sizes from SEM images are mainly in good agreement with the particle sizes calculated by Scherrer's equation and that obtained by TEM.

3.4 FTIR analysis

The FTIR spectra in the range of 4000–400 cm^{-1} of $Mn_xNa_{0.5}Co_{(0.5-x)}Fe_2O_4$ (where $x=0.1$, 0.3, and 0.5) nano-magnetic particles, calcined at 800 °C for 3 h, are revealed in Fig. 4. FTIR peaks $\sim$3457 cm^{-1} and 1633 cm^{-1} are originated because of the stretching and bending vibrations of (OH) molecules, which indicate the remnants of hydroxyl groups from the KBr pellet [30]. A feeble band at 1387 cm^{-1} is initiating due to some residual nitrate group in the prepared nanomagnetic samples [31]. There is a weak absorption peak at 2365 cm^{-1} in the FTIR spectra was recognized to the stretching vibration mode of C–H bond from some residual solvents [32]. The Na-CFO nanoparticles have the absorption band at 1115 cm^{-1} that moved to the low wavenumber values (1079 cm^{-1}) by the incorporation of Mn ions, which might be owing to the vibrations of the bond between the octahedral metal ion and oxygen ion [33]. Also, Fig. 4 shows two basic

Fig. 3 SEM images of $Mn_xNa_{0.5}Co_{(0.5-x)}Fe_2O_4$ nanoparticles for **a** $x=0.0$, **b** $x=0.1$, and **c** $x=0.3$, and **d** $x=0.5$ calcined at 800 °C
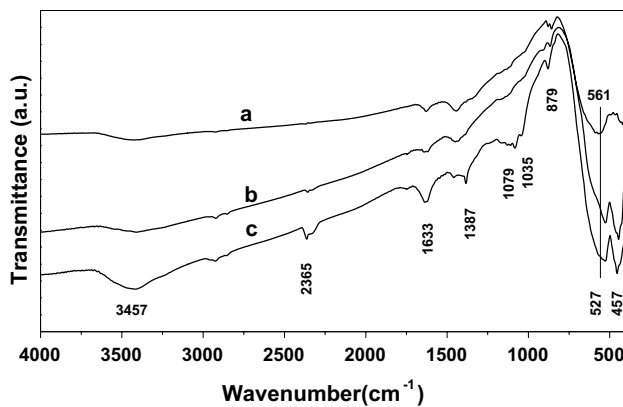
Fig. 4 FTIR spectra of $Mn_x Na_{0.5}Co_{(0.5-x)}Fe_2O_4$ nanoparticles for a $x = 0.1$, b $x = 0.3$, and c $x = 0.5$, calcined at 800 °C

absorption bands in the range of 600–400 cm^{-1} in which the first band is around 561 cm^{-1} and 527 cm^{-1} which resembles vibration of tetrahedral metal–oxygen bond and the second band is around 457 cm^{-1} which arises from stretching vibration of metal–oxygen bond at octahedral sites, which indicates the successful formation of cubic spinel nanostructure of Mn co-doped Na-CFO. The band shift to the lower frequency side with the incorporation of Mn ions may be explained by the incorporation of Mn^{2+} ions with a larger ionic radius inside the tetrahedral lattice sites (A). The shift resulted in the higher band only indicates the change in the bond length between the oxygen ions and metal ions at A-sites in the prepared spinel structure [34]. The absorption band at 500–600 cm^{-1} was attributed to stretching vibrations of Fe^{3+}-O^{2-} tetrahedral site, which was seemed in most of the nano-ferrite matrices.

3.5 Optical band gap

The behavior of the optical absorption of materials generally has a high rise at a convinced energy value that is related to the electron transition through the energy bands [18, 35, 36]. In many substances, the values of indirect type are lower than those of direct type. The equation that relates the absorption coefficient (α) to the incident photon frequency (ν) is represented by

$$\alpha = A(h\nu - E_g)^{n/2}/h\nu$$

where n is a constant equal to 1 for direct and 4 for indirect band gap transitions.

From the diffused reflected light in a dense material, the absorption coefficient can be calculated by Kubelka–Munk formula [37]:

$$KM = (1 - r)(1 - r)/(1 + r)$$

where r is referred to as I_0/I.

The $Mn_xNa_{0.5}Co_{(0.5-x)}Fe_2O_4$ (where $x = 0.0$, 0.1, 0.3, and 0.5) prepared by sol–gel autocombustion method were optically inspected by diffuse reflection (R) approach at room temperature. As represented in Fig. 5, the band gaps calculated by the KM formula of $Mn_xNa_{0.5}Co_{(0.5-x)}Fe_2O_4$ (where $x = 0.0$, 0.1, 0.3, and 0.5) take the values of 4.49, 4.45, 3.75, and 3.68 eV, respectively, and associated with indirect allowed type of transition [35]. The resulted band gap data show a decreasing behavior with increasing Mn dopant level. Many studies found that the band gap is increased to higher values with doping by Mn [38–44], and this was explained as a result of lattice distortion due to ionic radius difference which reduces the symmetry of the third orbital [45–47]. Only a few studies found that the Mn doping reduces the band gap [48] due to the existence of higher valence states of Mn (+3 or +4) which develop lattice defects [39, 49]. Also, another explanation of the reduction of band gap with the increasing Mn doping ratio may be due to the existence of a secondary phase [50, 51]. In all situations, the existence of Mn higher oxidation states is the direct reason for defect formation which leads to band gap reduction [52].

3.6 Magnetic properties

Vibrating sample magnetometer was used to evaluate the magnetic properties of $Na_{0.5}Mn_xCo_{(0.5-x)}Fe_2O_4$ (where x = 0.0, 0.1, 0.3 and 0.5) samples calcined at 800 °C for 3 h. The characteristic hysteresis loops for the prepared nanomagnetic particles are displayed in Fig. 6 which shows the dependency of explicit saturation magnetization on the magnetic system compositions. M–H loops of the prepared Na–cobalt ferrite and doped with Mn ions at room temperature indicate the ferromagnetic nature of the prepared highly porous nanostructures. Starting the hysteresis loops, the saturation magnetization (M_s), coercivity (H_c), and magnetic retentivity (M_r) for the prepared nanomagnetic Mn-doped Na-CFO samples are (61.404, 64.55, 48.45, and 37.15 emu g^{-1}), (706.45 Oe, 540.54 Oe, 439.19 Oe, and 337.84 Oe), and (20.155, 20, 15.6, and 8.4 emu g^{-1}), respectively. The magnetization depends on the cation distribution among A- and B-locations. The spin of both the locations couples antiferromagnetically leading to a clear magnetic moment, which is basically a numerical difference among sublattice magnetizations. Also, this behavior is might be due to strain-induced magnetization, where the magnetic networks are disturbed by the incorporation of Mn^{2+} ions in Na-CFO and the maximum enhancement of magnetic properties (ηB, as observed in Table 2) for the replacement of the magnetic Mn cations in place of Co can be obtained for $x = 0.1$ substitutions. The decrease in (M_s) values with the higher concentrations of Mn^{2+} ions can be recognized to the effect of the secondary hematite phase on saturation magnetization which is clarified on the basis of the spin canting
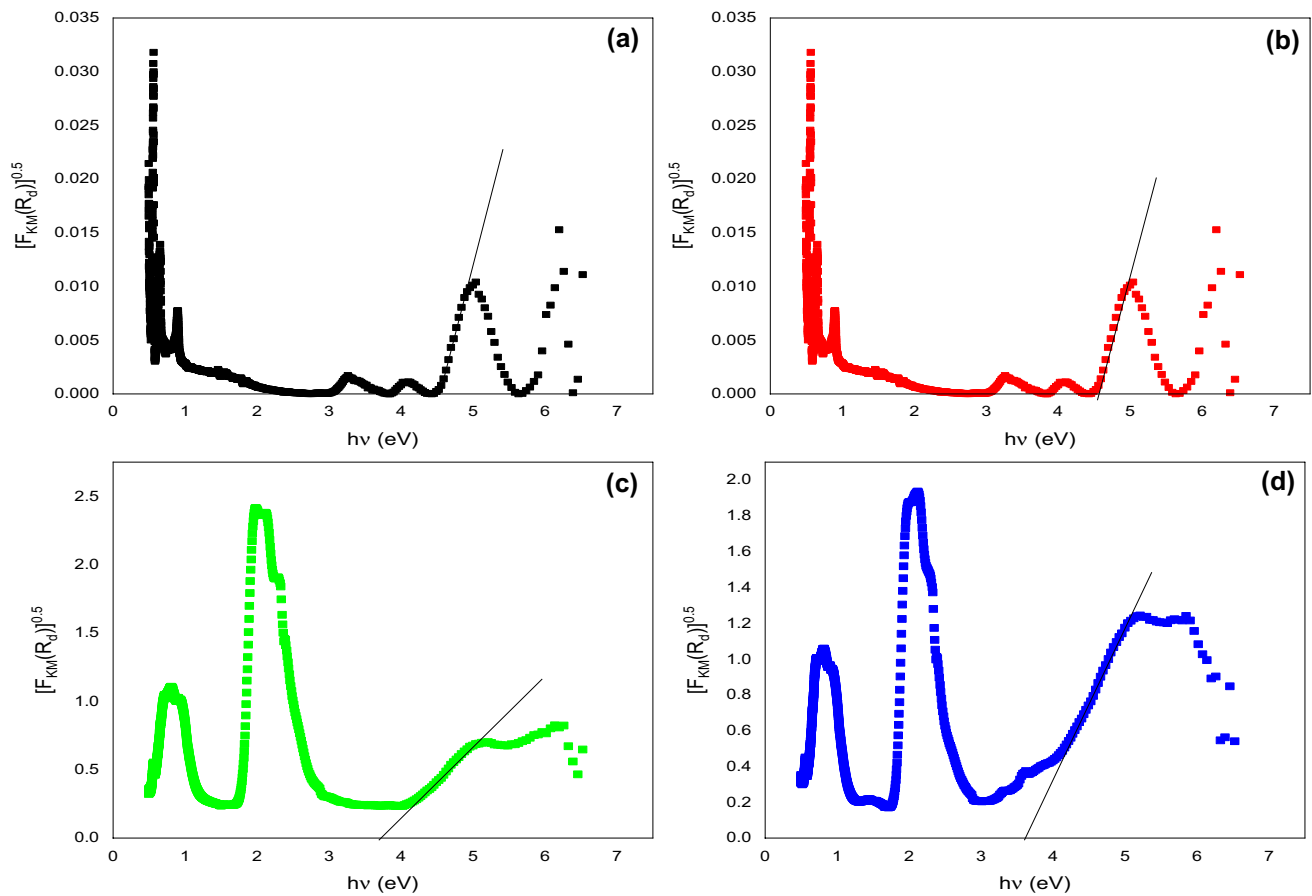
Fig. 5 Kubelka–Munk function of $Mn_x Na_{0.5}Co_{(0.5-x)}Fe_2O_4$ nanoparticles for **a** $x=0.0$, **b** $x=0.1$, and **c** $x=0.3$, and **d** $x=0.5$ calcined at 800 °C
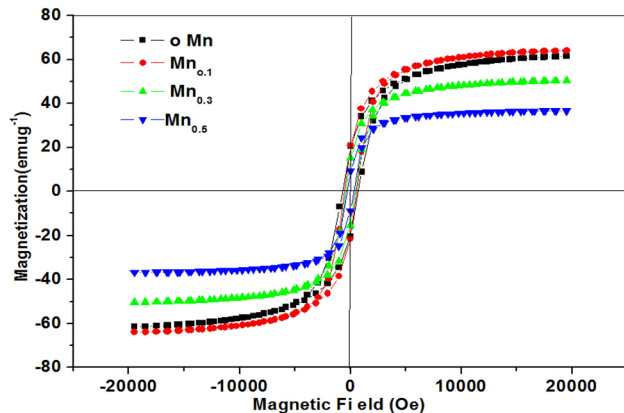
Fig. 6 Magnetic hysteresis loops of the samples Na-CFO and $Mn_xNa_{0.5}Co_{(0.5-x)}Fe_2O_4$ nanoparticles ($x=0.0$, 0.1, 0.3, and 0.5), calcined at 800 °C

effect. The interaction of the ferromagnetic spinel phase with antiferromagnetic hematite phase reasons predominant spin canting and the decreases in the total magnetic moment. Consequently, this decreases the (Ms) values in the prepared

matrix [53]. Also, cubic cobalt ferrite-based has an inverse-spinel structure, which has different cation distribution between (A) site-tetrahedral and (B) site-octahedral in which Na, Mn, and Co occupy some of the octahedral locations while the trivalent Fe^{3+} occupies the remnant of the octahedral locations and the other occupies tetrahedral site; so the resulted magnetic moment of Na–Mn–CFO is owing to the total spin moments of Na–Mn–Co in some octahedral site because they are aligned in one direction which decreases the magnetic effect of Na-CFO nanomagnetic [54, 55].

The higher the content of hematite secondary phases in spinel nano-ferrite particles, the higher the spin canting effect that leads to a decrease in the total magnetic moment (ηB) of the system. The remnant ratio $(R) = (Mr/Ms)$ is the characteristic parameter of a material. It is an indication of the simplicity with which the route of magnetization is reoriented toward the nearest easy axis magnetization direction after the magnetic field is uninvolved. The decrease in the coercivity may be correlated to the decreasing anisotropy of the cobalt ferrite system. It is clearly seen that the coercive force tends to decrease with the increase of Mn ions. Generally, coercivity depends

Table 2 Magnetic properties, Saturation magnetization (M_s), Coercivity (H_c), Remnant magnetization (M_r), Squareness (M_r/M_s), and Bohr magneton (η_B) of obtained Mn-Doped Na-CFO nanoparticles

Sample	M_s (emu/g)	M_r (emu/g)	H_c (Oe)	Squareness (M_r/M_s)	η_B
$Na_{0.5}Co_{0.5}Fe_2O_4$	61.404	20.155	706.45	0.32824	2.3820
$Mn_{0.1}Na_{0.5}Co_{0.4}Fe_2O_4$	64.55	20	540.54	0.30984	2.4995
$Mn_{0.3}Na_{0.5}Co_{0.2}Fe_2O_4$	48.45	15.6	439.19	0.32198	1.8691
$Mn_{0.5}Na_{0.5}Fe_2O_4$	37.15	8.4	337.84	0.22611	1.4279

on some factors, such as strain, grain size, magneto-crystallinity, morphology, anisotropy, and crystal phase [56]. In XRD analyses, the secondary phase is detected at the higher contents of Mn, which decreases the coercivity values [57, 58].

The squareness ratio value of the prepared composition is less than 0.5, which points to the uniaxial anisotropy contribution of internal strains in standard magnetic materials. This uniaxial anisotropy in magnetic nanoferrites occurred as a result of surface effects [59]. The magnetic behavior of Mn-substituted Na–cobalt nanoferrites showed soft magnetic characteristics which make them good candidates for application in opto-magnetic and microwave devices [60].

4 Conclusions

Nanostructure Mn co-doped $Na_{0.5}Mn_xCo_{(0.5-x)}Fe_2O_4$ (where $x = 0.0, 0.1, 0.3$, and 0.5) were synthesized through sol–gel autocombustion method. The XRD result of Mn co-doped Na-CFO suggests the successful formation of a single-phase spinel cubic structure with a space group (Fd3m). The diffuse reflection analysis shows that Mn co-doped Na-CFO has indirectly allowed band gaps and their values were extracted. Magnetic analyses indicate that the magnetic properties of Mn co-doped Na-CFO mainly depend on the compositions. Incorporation of Mn^{2+} ions can improve the M_s and coercivity of the Na-CFO matrix. The decrease in the coercivity may be correlated to the decreasing anisotropy of the cobalt ferrite system. The magnetic behavior of Mn-substituted Na–cobalt nanoferrites displayed soft magnetic characteristics that make them good candidates for high-density magnetic recording, energy storage, catalysis, magnetic resonance imaging, and microwave applications.

Compliance with ethical standards

Conflict of interest The authors declare that they have no conflict of interest.

References

1. L.H. Reddy, J.L. Arias, J. Nicolas, P. Couvreur, Chem. Rev. **112**, 5818 (2012)
2. C. Fernandes, C. Pereira, M.P. Fernández-García, A.M. Pereira, A. Guedes, R. Fernández-Pacheco, A. Ibarra, M.R. Ibarra, J.P. Araújo, C. Freire, J. Mater. Chem. C **2**, 5818 (2014)
3. I. Ali, Chem. Rev. **112**, 5073 (2012)
4. F. Hu, Y.S. Zhao, Nanoscale **4**, 6235 (2012)
5. J. Gass, H. Srikanth, N. Kislov, S.S. Srinivasan, Y. Emirov, J. Appl. Phys. **2008**, 103 (2008)
6. D. Zhang, C. Zhou, Z. Sun, L.Z. Wu, C.H. Tung, T. Zhang, Nanoscale **4**, 6244 (2012)
7. W. Wang, S.P. Gumfekar, Q. Jiao, B. Zhao, J. Mater. Chem. C **1**, 2851 (2013)
8. O. Vozniuk, T. Tabanelli, N. Tanchoux, J.M.M. Millet, S. Albonetti, F. Di Renzo, F. Cavani, Catalysts **8**, 332 (2018)
9. E. McCalla, C.M. Lowartz, C.R. Brown, J.R. Dahn, Chem. Mater. **25**, 912 (2013)
10. I. Sharifi, H. Shokrollahi, S. Amiri, J. Magn. Magn. Mater. **324**, 903 (2012)
11. S. Amiri, H. Shokrollahi, Mater. Sci. Eng. C **33**, 1 (2013)
12. J. Mohapatra, A. Mitra, D. Bahadur, M. Aslam, CrystEngComm **15**, 524 (2013)
13. A.J. Rondinone, A.C.S. Samia, Z. John Zhang, J. Phys. Chem. B **104**, 7919 (2000)
14. S. Sun, H. Zeng, D.B. Robinson, S. Raoux, P.M. Rice, S.X. Wang, G. Li, JACS **4**, 126 (2004)
15. J.T. Jang, H. Nah, J.H. Lee, S.H. Moon, M.G. Kim, J. Cheon, Angew. Chemie **48**, 1234 (2009)
16. I.H. Gul, W. Ahmed, A. Maqsood, J. Magn. Magn. Mater. **320**, 270 (2008)
17. A.M. El Nahrawy, A.B.A. Hammad, A.M. Youssef, A.M. Mansour, A.M. Othman, Appl. Phys. A **125**, 46 (2019)
18. A.M. El Nahrawy, A.M. Mansour, A.B. Abou Hammad, A.R. Wassel, Mater. Res. Express. **6**, 016404 (2019)
19. A.M. El Nahrawy, A.A. Soliman, E.M.M. Sakr, H.A. El Attar, J. Ovonic Res. **14**, 193 (2018)
20. B.A. Hemdan, A.M. El Nahrawy, A.M. Mansour, A.B.A. Hammad, Environ. Sci. Pollut. Res. **26**, 9508 (2019)
21. A.M. El-Nahrawy, A.I. Ali, A.B. Abou Hammad, A.M. Youssef, Int. J. Biol. Macromol. **93**, 267 (2016)
22. C.Y. Tsay, Y.C. Chiu, C.M. Lei, Materials (Basel). **11**, 2274 (2018)
23. P. Hu, H.B. Yang, D.A. Pan, H. Wang, J.J. Tian, S.G. Zhang, X.F. Wang, A.A. Volinsky, J. Magn. Magn. Mater. **322**, 173 (2010)
24. S.A.V. Prasad, M. Deepty, P.N. Ramesh, G. Prasad, K. Srinivasarao, C. Srinivas, K. Vijaya Babu, E. Ranjith Kumar, N. Krisha Mohan, D.L. Sastry, Ceram. Int. **44**, 10517 (2018)
25. M. Deepty, C. Srinivas, K. Vijaya Babu, E. Ranjith Kumar, S. Singh Meena, C.L. Prajapat, N. Krisha Mohan, D.L. Sastry, J. Magn. Magn. Mater. **466**, 60 (2018)

26. E. Ranjith Kumar, R. Jayaprakash, M.S. Seehra, T. Prakash, S. Kumar, J. Phys. Chem. Solids **74**, 943 (2013)
27. M.A. Almessiere, Y. Slimani, M. Sertkol, M. Nawaz, A. Sadaqat, A. Baykal, I. Ercan, B. Ozçelik, Nanomaterials **9**, 3 (2019)
28. M.H. Abdellatif, G.M. El-Komy, A.A. Azab, J. Magn. Magn. Mater. **442**, 445 (2017)
29. R. Ali, M. Azhar Khan, A. Manzoor, M. Shahid, M. Farooq Warsi, J. Magn. Magn. Mater. **441**, 578 (2017)
30. A.M. Youssef, A.M. El-Nahrawy, A.B. Abou Hammad, Int. J. Biol. Macromol. **97**, 561 (2017)
31. H.S. Mund, B.L. Ahuja, Mater. Res. Bull. **85**, 228 (2017)
32. A. Baykal, S. Esir, A. Demir, S. Güner, Ceram. Int. **41**, 231 (2015)
33. A. Baykal, N. Kasapoğlu, Y. Köseoğlu, M.S. Toprak, H. Bayrak-dar, J. Alloys Compd. **464**, 514 (2008)
34. K. Kumar, A. Loganathan, Mater. Chem. Phys. **214**, 229 (2018)
35. A.M. Mansour, Silicon **11**, 1 (2018)
36. A.A.M.A.M.M. Farag, W.G.G. Osiris, A.H.H. Ammar, A.M.M. Mansour, Synth. Met. **175**, 81 (2013)
37. P. Komulainen, in *Biermann's Handb. Pulp Pap.* (Elsevier, 2016), pp. 1–60.
38. R. Rajesh Kanna, N. Lenin, K. Sakthipandi, M. Sivabharathy, Ceram. Int. **43**, 15868 (2017)
39. S. Husain, L.A. Alkhtaby, E. Giorgetti, A. Zoppi, M. Muniz Miranda, J. Lumin. **145**, 132 (2014)
40. H. B. Ruan, L. Fang, D. C. Li, M. Saleem, G. P. Qin, C. Y. Kong, in *Thin Solid Films* (2011), pp. 5078–5081.
41. M. Amin, U. Manzoor, M. Islam, A.S. Bhatti, N.A. Shah, Sensors (Switzerland) **12**, 13842 (2012)
42. B. Babukutty, N. Kalarikkal, S.S. Nair, Mater. Res. Express **4**, 035906 (2017)
43. F. Rubio-Marcos, A. Quesada, M.A. García, M.A. Bañares, J.L.G. Fierro, M.S. Martín-Gonzalez, J.L. Costa-Krämer, J.F. Fernández, J. Solid State Chem. **182**, 1211 (2009)
44. M. Z. Ahsan, *Study on Effects of Mn Substitution in Cobalt Ferrite* (n.d.).
45. Ü. Özgür, Y. I. Alivov, C. Liu, A. Teke, M. A. Reshchikov, S. Doğan, V. Avrutin, S. J. Cho, H. Morkoç, J. Appl. Phys. **98**, 1 (2005).
46. P.A. Rodnyi, I.V. Khodyuk, Opt. Spectrosc. (English Transl. Opt. i Spektrosk. **111**, 776 (2011)
47. M. Peiteado, S. Sturm, A.C. Caballero, D. Makovec, Acta Mater. **56**, 4028 (2008)
48. D.P. Joseph, C. Venkateswaran, J. Atom. Mol. Opt. Phys. **2011**, 1 (2011)
49. L. Schmidt-Mende, J.L. MacManus-Driscoll, Mater. Today **10**, 40 (2007)
50. S. Guo, Z. Du, S. Dai, Phys. Status Solidi Basic Res. **246**, 2329 (2009)
51. D.P. Dubal, D.S. Dhawale, R.R. Salunkhe, S.M. Pawar, C.D. Lokhande, Appl. Surf. Sci. **256**, 4411 (2010)
52. S. Sharma, P. Ramesh, P. Swaminathan, J. Electron. Mater. **44**, 4710 (2015)
53. S. Hajarpour, A. Honarbakhsh Raouf, K. Gheisari, J. Magn. Magn. Mater. **363**, 21 (2014)
54. M. Zawrah, M. El-Okr, A. Ashery, A. A. H.-M. E. J. Appl. 2016 (n.d.).
55. A.B. Abou Hammad, M.E. Abd El-Aziz, M.S. Hasanin, S. Kamel, Carbohydr. Polym. **216**, 54 (2019)
56. R. Tholkappiyan, K. Vishista, Mater. Sci. Semicond. Process. **40**, 631 (2015)
57. P. Samoila, L. Sacarescu, A.I. Borhan, D. Timpu, M. Grigoras, N. Lupu, M. Zaltariov, V. Harabagiu, J. Magn. Magn. Mater. **378**, 92 (2015)
58. C. Murugesan, G. Chandrasekaran, RSC Adv. **5**, 73714 (2015)
59. R. Tholkappiyan, K. Vishista, Appl. Surf. Sci. **351**, 1016 (2015)
60. K.K. Kefeni, T.A.M. Msagati, B.B. Mamba, Mater. Sci. Eng. B **215**, 37 (2017)